High resolution electron spin resonance microscopy

Aharon Blank, Curt R. Dunnam, Peter P. Borbat, and Jack H. Freed*

National Biomedical Center for Advanced ESR Technology, Department of Chemistry and Chemical Biology, Cornell University, Ithaca, NY 14853, USA

Abstract

NMR microscopy is routinely employed in fields of science such as biology, botany, and materials science to observe magnetic parameters and transport phenomena in small scale structures. Despite extensive efforts, the resolution of this method is limited ($>10\,\mu m$ for short acquisition times), and thus cannot answer many key questions in these fields. We show, through theoretical prediction and initial experiments, that ESR microscopy, although much less developed, can improve upon the resolution limits of NMR, and successfully undertake the $1\,\mu m$ resolution challenge. Our theoretical predictions demonstrate that existing ESR technology, along with advanced imaging probe design (resonator and gradient coils), using solutions of narrow linewidth radicals (the trityl family), should yield 64×64 pixels 2D images (with z slice selection) with a resolution of $1 \times 1 \times 10\,\mu m$ at $\sim 60\,GHz$ in less than 1 h of acquisition. Our initial imaging results, conducted by CW ESR at X-band, support these theoretical predictions and already improve upon the previously reported state-of-the-art for 2D ESR image resolution achieving $\sim 10 \times 10\,\mu m$, in just several minutes of acquisition time. We analyze how future progress, which includes improved resonators, increased frequency of measurement, and advanced pulsed techniques, should achieve the goal of micron resolution.
© 2003 Elsevier Inc. All rights reserved.

Keywords: ESR imaging; ESR microscope; Trityl radical; Gradient coils; High permittivity resonator

1. Introduction

NMR microscopy is a well-established field of science, which employs the techniques of MRI with large gradients in high magnetic fields to enable high image resolution [1]. The state-of-the-art of today's NMR microscope achieves voxel resolution of $\sim[3.5\,\mu m]^3$ in a liquid, at a frequency of 400 MHz after $\sim 30\,h$ of data acquisition [2]. NMR microscopy in the solid state achieves voxel resolution of $\sim[150\,\mu m]^3$ [3,4] and also requires several hours of data acquisition. Commercial NMR microscopes are available from several vendors and are used for characterization of tissues with fine structures, non-invasive tracing of plant metabolism, investigation of transport phenomena, histological-like applications and more [5,6]. While the field of NMR microscopy is well developed, ESR microscopy is a largely unexplored area. Most of the efforts with respect to ESR imaging are directed towards imaging of large biological objects [7–10] and determining the radical and oxygen concentration (by its effect on the radical linewidth). Such experiments, conducted *in-vivo*, employ low fields of $\sim 10\,mT$ at low RF frequencies, where the RF energy penetrates well into the biological object. Consequently, a typical voxel resolution in low frequency ESR experiments is ca. $[2\,mm]^3$. Most of the low field imaging techniques are based on CW detection while applying static gradients in various directions with respect to the object (the so-called back-projection technique). However, some techniques use a single pulse FID sequence in conjunction with pulsed and static gradients [10].

In contrast to the recent advances in low frequency ESR imaging, high frequency ESR imaging, directed to microscopy, is not well developed. The reasons may be a combination of technical difficulties and the lack of scientific interest. In our opinion, the main problem is that above a certain "threshold" of reasonable imaging time (several minutes to an hour) and without having a

---

* Corresponding author. Fax: 1-607-255-6969.
E-mail address: jhf3@cornell.edu (J.H. Freed).

minimal appropriate spatial resolution ($\sim$1–10 μm), the range of potential applications is limited. Thus, for example, only when a sub-cellular resolution is achieved (where human cells typically range in size from 10 to 100 μm), one can have unique information based on the ESR imaging technique, which may further advance biophysical research. As we shall see below, ESR imaging at sub-cellular resolution, in acceptable measurement time is challenging, since it requires the use of advanced resonators, state-of-the-art data acquisition techniques, highly efficient gradient coils, and the use of unique radicals that have long T_2s and are stable in biological/botanical specimens. Thus, all these challenges must be addressed in order to achieve (sub)micron resolution, and thereby make of ESR microscopy a viable analytical tool.

At this point, we summarize the key accomplishments that were achieved in the past with respect to high resolution ESR imaging. In CW techniques, the modulated field gradient method [11] is best suited for microscopic purposes due to its relatively small image artifacts and the low sensitivity to nonlinearity of the gradients, as compared to the more common projection reconstruction method. Employing the modulated field gradient method, a resolution better than $\sim$10 μm was achieved in one dimension [11,12], whereas 2D images exhibit resolution of $\sim[100\,\mu m]^2$ [13]. The CW technique with static magnetic field gradients, achieved a resolution of $\sim$10 μm for 1D experiments [14] and the 2D resolution, employing CW with projection reconstruction, is of the order of $\sim[100\text{–}200\,\mu m]^2$ [15].

Pulsed ESR imaging techniques require fast gradient switching and spin probes with sufficiently long T_2. Key work in pulsed high resolution ESR microscopy was therefore conducted with a $(FA)_2X$ crystal, which is a unique organic conductor, having T_2 of $\sim$6 μs at room temperature. Using this material, one-dimensional imaging with $\sim$10 μm resolution was reported for pulsed X-band [16]. Low-frequency pulse RF ESR, employing standard NMR microscopy gradients, achieved 2D and 3D images with resolution of $\sim[20\text{–}30\,\mu m]^3$ [17,18] after $\sim$10 h of data acquisition. The unique crystals used in these experiments and the long acquisition time for 2D/3D images are not attractive for biophysical, botanical, and many other potential applications. An early 1D imaging work at high field (5 T, 140 GHz) achieved a resolution of $\sim$200 μm, limited by the gradient system [19]. One should also note the early efforts in pulsed X-band spin-echo imaging [20].

Other new methods for magnetic resonance detection, applicable to imaging, include Hall detection [21], miniature microwave scanning probe [22], magnetic force detection [23], and STM-ESR [24]. The first two methods operate at the micron scale but both have rather low spin sensitivity, with the second method suffering from non-symmetrical image resolution. The third and especially the fourth methods feature high detection sensitivity, but operate at the nanometer/single molecule regime, rather than at the micron scale. Consequently they require unique sample preparation methods, are too fine grained, and thus, not useful for most of the applications discussed here.

In this study we present some of the reasons to strive for high resolution ESR microscopy. We describe the theoretical limitations and the technical problems in achieving high resolution ESR images and present our preliminary experimental efforts. At this stage of development, we have obtained 2D images with a resolution of $\sim[10\,\mu m]^2$ employing the modulated field gradient method. In contrast to the previous work on ESR microscopy noted above, which dealt with high spin concentration phantoms, we focus our theoretical and experimental efforts on samples with low spin concentrations in solution. These are more relevant for the applications discussed here. Nevertheless, we do present some imaging examples of high spin concentration phantoms, which help to characterize our system's capabilities.

2. Research motivation

Of a number of applications that can benefit from the development of an ESR-based microscope, we mention just a few:

1. Measurements of oxygen concentration in model systems and living cells [9]: The concentration of oxygen is one of the most important variables in many physiological, pathological, and therapeutic processes. As the terminal acceptor in the electron transport chain, O_2 plays a critical role in cellular metabolism. ESR imaging techniques can indirectly measure O_2 concentration via its effect on the radical linewidth.

2. Sub-cellular resolution of in vitro molecular imaging: Molecular magnetic resonance imaging (termed mMRI) is an emerging field, which exploits the capabilities of commercially available MRI and NMR microscopy systems together with newly synthesized contrast agents, that attach to a specific molecule or genetic sequence of interest and enable one to identify its presence and location [25–27]. This field of research has applications ranging from medicine and biology to botany and chemistry. The availability of an ESR microscopy technology would certainly stimulate new applications based on the use of paramagnetic probes. The probes, which would attach to the molecules of interest, will enable far greater spatial resolution due to the high ESR spin sensitivity and the avoidance of an unwanted signal from the bulk of the sample, (e.g., water in NMR).

3. Functional imaging of plants [28]: NMR has been used extensively in botany to examine issues such as

water diffusion and distribution of metabolites. Similar functions can be addressed by ESR imaging, after treating the plant with an appropriate radical solution. Many aspects of plant science can be explored without the addition of stable radicals, since radicals are produced in plants naturally in a number of processes, such as fungal infection [28]. ESR imaging techniques were used to observe natural humic substance radicals in seeds [29]. In addition, ESR studies have been undertaken to determine plant membrane permeability [30]. Imaging methods in plants are performed, for example, in conjunction with genetically transformed plants to study the changes in metabolic pools or changes in water flow arising from altered protein expression.

4. Imaging of radiation effects: ESR imaging has been used for a long time in dosimetry and for assessment of radiation damage in bones [31], and tooth enamel [32]. The information obtained by ESR imaging enables one to determine the spatial distribution of the effects caused by radiation, as well as to determine possible inhomogeneities in the imaged structure. Improved spatial resolution would reveal the effects of ionizing radiation on a fine scale that is of special interest in this research area [33,34].

5. ESR imaging of chemical reactions: ESR imaging has been used to evaluate polymer degradation [35,36], to enable in situ observation of spatial distribution of paramagnetic species (such as reactants, products, and intermediates) in catalyst systems, monitor the diffusion in a catalyst pellet, and characterize the poisoning in micro fixed-bed reactors [37]. In addition, ESR imaging was used to explore other chemically related processes such as annealing under a thermal gradient [38]. Again, this line of research would be likely to benefit from the availability of an ESR-based microscope with enhanced sensitivity and improved spatial resolution.

6. ESR imaging of microviscosity in living cells: The effect of microviscosity differences may be the basis for several physiological differences between tumors and normal tissues, with the likelihood of stimulating a higher growth rate in tumor tissue. ESR has been successfully applied to characterize such effects [39]. In a similar application, ESR imaging has been used to evaluate in vitro the permeability of dental hard tissue to water [40]. Extensive research has also been conducted employing micro ESR imaging (20 μm 1D resolution) for the evaluation of radical diffusion in human skin, providing information about the micro- and macromolecular environments [12]. Similar and more elaborate studies can benefit from the proposed microscope, especially from the ability to apply high amplitude pulsed gradient spin-echo methods, which yields the diffusion constants of the imaged substance [1].

7. ESR imaging in materials science: Several important applications in materials science have already been addressed by ESR imaging [41]. These include, for example, 1D ESR imaging of conducting and lossy-dielectric samples [42], an ESR imaging study of the distribution of paramagnetic centers in thiokol–epoxy hermetics [43], the study of material porosity [44], observation of diamond defects [45], and analyzing polymers and other solid material [46]. This vast field of application relies both on the detection of naturally occurring free radicals and radicals which are administrated as part of the imaging process.

8. "Traditional" NMR microscopy applications: In addition to all the above-mentioned applications, ESR microscopy has the potential of being used in areas currently addressed only by NMR microscopy. The increased resolution of the proposed microscope would make the ESR-based method more attractive for the investigation of issues such as "histological-like" applications [6], studies of flow in biological, botanical, and other media [47], medical-clinical related *in-vitro* measurements of cartilage degenerative diseases [48], and a combination of fluorescence optical microscopy and NMR microscopy for inspection of cells [49].

The above applications represent only some examples from the wide literature on the subject. The bottom line is that ESR microscopy is currently insufficiently developed: it certainly is not available commercially, and it provides the potential user with only limited resolution and sensitivity. The development of adequate ESR microscope technology would likely stimulate additional applications, which are hard to predict at the present time, just as is often the case with the introduction of new technologies.

3. The theoretical limitations of ESR microscopy

We shall now examine theoretically the factors which determine the resolution in ESR microscopy experiments with respect to common CW and pulse techniques.

3.1. CW method

As was stated above, the preferred method to acquire the ESR image is the modulated field gradient method [11]. This method is based on applying modulated gradient fields on the sample in all imaged dimensions so that at every instant, only one voxel is subjected to a vanishing modulated field and all other voxels are over-modulated by the high amplitude modulation signal. The image is acquired by sequential change of the nodal point of the modulated fields, to enable acquisition of the signal from the various voxels of the sample. Using this method, there are basically two main limiting factors for image resolution: the single voxel signal-to-noise-ratio (SNR) and the amplitude of the gradient required to suppress the signal

from the non-imaged voxels. Let us quantitatively analyze these two factors.

For a linear detector and reflection resonator configuration, the CW ESR signal from a given voxel can be written as [50]

$$S_{CW} = \chi'' \eta Q_u \sqrt{PR_0}, \qquad (1)$$

where χ'' is the specific resonant susceptibility of the sample, η is the voxel filling factor, Q_u is the unloaded Q of the resonator, P is the incident microwave power, and R_0 is the impedance of the transmission line connecting the microwave source to the resonator. To maximize the signal of the voxel, the resonator effective volume, V_c, should be decreased (thus, increasing η) and/or P should be increased. However, each of these changes would result in increased microwave power within the resonator, leading to increased B_1. Eventually, the sample will become saturated, according to the expression

$$\chi'' = \chi_0'' \cdot s, \quad s = \frac{1}{1 + B_1^2 \gamma^2 T_1 T_2} = \frac{1}{1 + C_p^2 P \gamma^2 T_1 T_2}, \qquad (2)$$

where χ_0'' is the sample specific susceptibility at unsaturated conditions, γ is the electron gyromagnetic ratio, and C_p is the resonator power conversion factor (in $T/\sqrt{W}$), approximated for the average field in the rotating frame, as [50]

$$C_p \approx \sqrt{Q_L \mu_0 / V_c \omega_0}. \qquad (3)$$

Since at critical coupling the loaded Q of the resonator, $Q_L = Q_u/2$, and since η for a single voxel sample is inversely proportional to V_c, the following expression for the ESR signal, as a function of P and V_c, is obtained:

$$S_{CW} \approx \frac{\chi_0'' \eta_0 Q_u \sqrt{PR_0}}{V_c} \cdot \frac{1}{1 + (Q_u \mu_0 / 2V_c \omega_0) P \gamma^2 T_1 T_2}, \qquad (4)$$

where η_0 is the filling factor for a single voxel sample in a resonator with an effective volume of unity [51]. The SNR is obtained after dividing S_{CW} by the amplitude of the Johnson noise in a bandwidth Δf, $(4k_b T R_0 \Delta f)^{1/2}$ (resulting in the cancellation of R_0 in Eq. (4)). Practical SNR results, however, should include noise from all other sources and also consider the losses in the detection and amplification stages [50]. To a reasonable degree of approximation, both can be accounted for by considering thermal noise that is a factor of four greater than the ideal Johnson noise. Thus,

$$SNR_{CW} \approx \frac{\chi_0'' \eta_0 Q_u \sqrt{P}}{8 V_c \sqrt{k_b T \Delta f}} \cdot \frac{1}{1 + (Q_u \mu_0 / 2V_c \omega_0) P \gamma^2 T_1 T_2}. \qquad (5)$$

Fig. 1 presents two examples for the calculated SNR as a function of the resonator active volume, using the above expressions for X- and Q-bands, for a $[1\,\mu m]^3$ sample, placed at the center of the resonator.

Although the ultimate limiting factor in terms of image resolution in the CW method is the SNR, the resolution is also determined by the effectiveness of the
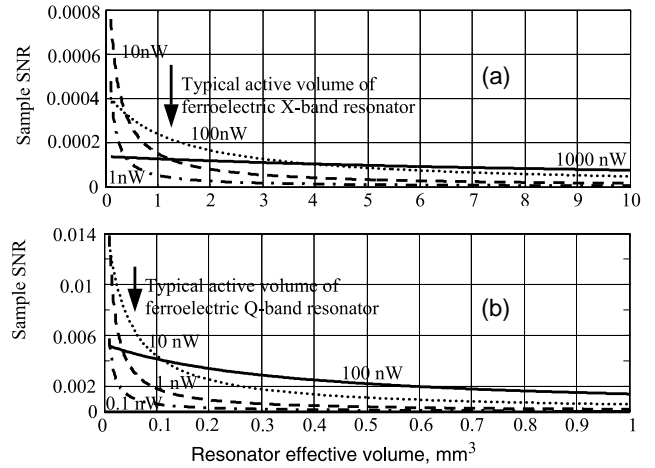

Fig. 1. (a) Calculated CW X-band SNR for a $1\,[\mu m]^3$ deoxygenated sample of protonated trityl radical (Tris(8-carboxyl-2,2,6,6-tetramethylbenzo-[1,2-d;4,5-d']bis[1,3]dithiol-4-yl)tri-sodium salt) in a concentration of 1 mM, and viscosity of 1 cP (cf. Eq. (5)). The calculations were performed for different values of the applied microwave power, as marked on the figure and represented by the different line styles. The values of $T_1 \sim 12.8$ and $T_2 \sim 3.3\,\mu s$ were determined employing a 17.2 GHz FT-ESR spectrometer [71] and were used throughout the calculations. Additional parameters taken in the calculation were $Q_u = 2000$; acquisition time constant of 0.1 s (i.e., $\Delta f = 10\,Hz$) and $T = 300\,K$. The sample volume contains $\sim 6 \times 10^5$ spins. (b) The same as in (a), but for Q-band. The vertical arrow indicates in both cases a typical active volume of the unique ferroelectric resonators employed in this work.

modulated gradient coils and therefore this factor should be considered in more detail. The image resolution for a first harmonic recorded spectrum, employing modulation amplitude equal to the FWHM of the ESR signal ($\Delta B_{1/2}$), is given by [11,50]

$$\Delta z \approx \frac{2\Delta B_{1/2}}{G_z}. \qquad (6)$$

Thus, for a radical with $\Delta B_{1/2} = 0.01\,mT$, a gradient of $G_z \sim 20\,T/m$ corresponds to 1 μm resolution. For the second harmonic signal, the resolution is a factor of ~ 2 better [52] (at the expense of signal amplitude). We can comment on the feasibility of obtaining such gradients by comparison with our current gradient system (described below) that for the X-band probe achieves a gradient of 2.5 T/m for 1 A of current and dissipates $\sim 8\,W$. This value corresponds to a resolution of $\sim 10\,\mu m$ for the trityl radical. For higher resolution one should consider smaller imaging probes (at 35 GHz or higher), which could improve significantly the gradient efficiency, B/I (that typically scales as $\sim 1/r^{3/2}$, where r is a typical distance from the coil to the sample) and reduce the power dissipation. It should also be noted that removal of heat dissipated by the gradient coils could be further improved, resulting in the possibility of increasing the gradients even further.

To summarize this part, in the CW method, the SNR of Eq. (5) is directly related to the resolution and will

probably be the limiting factor in terms of the achievable resolution. Our calculations (Fig. 1 and Eqs. (5) and (6)) lead to the following estimations: For 1 mM trityl-doped sample, one should obtain a 2D image, employing z slice selection, with 64×64 pixels in ~1 h of acquisition ($\Delta f = 1$ Hz implies acquisition time constant of 1 s per pixel, and this time is multiplied by the number of pixels), with a resolution of: X-band: ~$10 \times 10 \times 50\,\mu m$; Q-band: ~$2.5 \times 2.5 \times 25\,\mu m$; and U-band (60 GHz): ~$1.5 \times 1.5 \times 10\,\mu m$ (or ~$2.8 \times 2.8 \times 2.8\,\mu m$). The estimated voxel SNR is ~3 for all frequencies, and imaging time increases linearly with the number of voxels.

Extrapolation beyond 60 GHz is questionable, since at higher frequencies the current resonator assembly becomes too small to handle and the microwave technology is more limited in terms of the availability of low loss components. Also, the calculations assume that the radical relaxation times do not change much as frequency is increased. This assumption relies on previous measurements [53] performed at 1–10 GHz and our results at 17.2 GHz (cf. Fig. 1 caption). However, our initial measurements of T_1 and T_2 of this radical at W-band ($T_1 \approx 1\,\mu s$; $T_2 \approx 0.6\,\mu s$) indicate that this trend does not extend to higher frequencies, further affirming that one should be careful not to extrapolate too far.

It should also be noted that our theoretical estimations were made for 1 mM deoxygenated protonated trityl solution in water. Of course the SNR can be affected by the changes of relaxation times caused by radical deuteration; variation of viscosity; Heisenberg exchange, significant at higher trityl concentrations; and relaxation due to paramagnetic impurities present in the specimen, e.g., oxygen. For example, deuterated trityl has longer T_2 [53]; higher viscosity will shorten T_2 [53]; Heisenberg exchange will shorten T_2 [54]; and oxygen lowers both T_1 and T_2 [54]. We will not elaborate on these effects in this work, which provides only rough estimates of the resolution achievable in ESR microscopy.

3.2. Pulse method

In a pulsed 3D imaging experiment, the SNR per voxel can be determined to a good approximation by dividing the SNR of the entire sample by the number of voxels (more accurate calculations are affected by details of the exact acquisition technique, the distribution of the magnetic fields in the resonator and the data processing techniques used to acquire the image [1], however, these "higher" order issues are not considered here). While the methodology for estimating the FID or echo signal in NMR is well established and validated [55–57], for pulsed ESR the situation requires slight adjustments of the existing formulas. The usual formula for the signal in the NMR literature gives the voltage produced in a coil with a

field efficiency (the field produced by a unit current), $\varepsilon = \boldsymbol{B}_1/I$, due to a precessing specific magnetization $\boldsymbol{M}$

$$S_{\text{pulse}} = \omega \int \boldsymbol{M} \cdot \boldsymbol{\varepsilon}. \tag{7}$$

From the voltage in the detection coil, we can use the equivalent circuit which describes the resonator's coupling to the detector and obtain the voltage in the detector, S_{pulse}^{β}, as [58,59]

$$S_{\text{pulse}}^{\beta} = \frac{\beta}{1+\beta} \sqrt{\frac{R_0}{\beta R}} S_{\text{pulse}}. \tag{8}$$

Here β is the coupling to the resonator and R is the resonator's equivalent resistance (used also later for noise calculations). Such formalism has been found useful for spin-echo SNR estimation for loop-gap resonators, for which B_1/I and R are well defined [58]. Let us look at the more general case, which can handle any ESR resonator (rectangular, cylindrical, dielectric, etc.) where it is not apparent what B_1/I corresponds to and what are the equivalent R and L of the resonator.

Every resonator can be represented by an equivalent RLC circuit, coupled to a transmission line. Following a pulse, the signal ζ in the equivalent receiving coil, induced by magnetization $\boldsymbol{m}$, is given by [60]

$$\zeta = \frac{\partial}{\partial t}(\boldsymbol{\varepsilon} \cdot \boldsymbol{m}). \tag{9}$$

On the other hand, the noise voltage is given by:

$$N = \sqrt{4k_b TR\Delta f}. \tag{10}$$

Thus, the signal-to-noise-ratio is

$$\begin{aligned} \text{SNR}_{\text{pulse}} &= \frac{(\partial/\partial t)(\boldsymbol{\varepsilon} \cdot \boldsymbol{m})}{\sqrt{4k_b TR\Delta f}} \\ &= \frac{1}{\sqrt{4k_b T\Delta f}} \frac{\partial}{\partial t}\left(\frac{\boldsymbol{\varepsilon}}{\sqrt{R}} \cdot \boldsymbol{m}\right). \end{aligned} \tag{11}$$

As noted above, the field efficiency, $\boldsymbol{\varepsilon}$, corresponds to the magnetic field in the resonator due to 1 A of current. This quantity is difficult to measure for an arbitrary resonator, however, we do know that 1 W of power entering the resonator, under matched conditions, would result in an effective RMS current of $I = 1/\sqrt{R}$ produced in the equivalent RLC circuit representing the resonator. Thus, it is clear that the *amplitude* of the B_1 field in the *laboratory frame* produced by this 1 W of power is $\sqrt{2/R}\varepsilon$, and thus the field produced in the *rotating frame* is (we avoid from here, for simplicity, the vector notation of $\boldsymbol{\varepsilon}$, and assume it is only along one of the transverse axes of the laboratory frame of reference)

$$\frac{1}{\sqrt{2}}\left(\frac{\varepsilon}{\sqrt{R}}\right) \equiv C_{\text{p}}. \tag{12}$$

The value of C_{p}, can be measured by standard pulse techniques [50] or calculated using Eq. (3). By substituting Eqs. (3) and (12) in Eq. (11) and integrating over

the entire active volume of the resonator (notice that the magnetization $\boldsymbol{m}$ is only for a point sample and that we ignore slight differences between the filling factor calculation for CW and pulsed experiments resulting in slightly different active volumes [61]), we can obtain the following approximation for the FID/echo SNR (again considering four times more noise than the theoretical thermal noise):

$$\mathrm{SNR}_{\mathrm{pulse}} \approx \frac{M\omega_0}{4\sqrt{4kT\Delta f}}V_c\sqrt{2}C_p \approx \frac{\sqrt{2\mu_0 V_c}\,\omega_0 M}{8\sqrt{kT\Delta f}}\sqrt{\frac{Q_L}{\omega_0}}.$$

(13)

Here, M can be considered as the average specific magnetization, which takes into consideration field inhomogeneity within the resonator.

From Eq. (13) it is apparent that the signal of the entire sample is directly proportional to the square root of the resonator volume. However, for a single voxel of constant volume (e.g. $[1\,\mu m]^3$), the SNR is proportional to the SNR of the entire sample, divided by the resonator volume. This means that the image SNR for a constant voxel volume is proportional to $1/\sqrt{V_c}$. Thus, exactly as in the CW case, to improve the voxel SNR, one has to decrease the resonator size as much as possible. Using the parameters for 1 mM trityl radical (cf. Fig. 1 caption), in an X-band resonator with active volume of $[1\,mm]^3$ and $Q_L = 500$ in Eq. (13), yields the single-shot SNR of ~ 5000, when the resonator is completely filled with the sample. This corresponds to single-shot SNR of $\sim 5 \times 10^{-6}$ for $[1\,\mu m]^3$ voxel. In one second of acquisition time, this low figure can be improved by a factor close to ~ 1000. This is achieved by $\sim 100\,K$–1 M averages per second, which is supported by today's state-of-the-art acquisition cards. Such an averaging scheme may be based upon a CPMG sequence [62] with ~ 10 echoes separated by $\sim 0.2\,\mu s$. This sequence can be repeated every T_1 ($\sim 10\,\mu s$ depending on O_2 concentration), resulting in a total of $\sim 10 \times 100\,K = 1\,M$ echoes in 1 s. It should be noted that these SNR results for pulsed X-band are ~ 10 times better than the ones calculated for the CW case (for 1 s of acquisition), but are still inadequate to provide $[1\,\mu m]^3$ resolution in a reasonable acquisition time.

Whereas the SNR is mainly concerned with the resonator and the radical properties, the gradients impose an additional, almost orthogonal, technical difficulty. The gradient system is closely related to the nature of the imaging experiment. Therefore, let us consider for example a typical imaging sequence, which is based on one constant gradient and two phase gradients [18]. Similar gradients are also suitable in the case of CPMG pulse sequences [63]. The requirement from the constant gradient is to satisfy the condition [16]

$$G_z = \frac{2}{\gamma \Delta z T_2}.$$

(14)

We would like to obtain high spatial resolution of at least $\sim 10\,\mu m$ along the z-axis of the sample (that is normally along the sample tube). Therefore, the required G_z, which can be kept constant, is $\sim 0.4\,T/m$ (for typical trityl radical parameters, see Fig. 1 caption). Such a gradient results in a signal broadening of $\sim 5\,MHz$ for a $\sim 0.4\,mm$ thick sample, corresponding to an echo width of ~ 100–200 ns. In addition to the constant z gradient, two x- and y-phase gradients should be applied. The phase gradients should satisfy the condition [1]

$$\Delta x = \frac{1}{2\gamma/2\pi \int_t G_x \, dt}.$$

(15)

In the short time regime, where a CPMG sequence would require gradients of length of the order of $\sim 100\,ns$, then $G_x \sim 20\,T/m$ in order to achieve 10 μm resolution. Such gradients impose a significant technical challenge, but are feasible based on our past experience [64,65] especially for the small resonators considered here. For 1 μm resolution one would have to use longer pulsed gradients, and thus reduce the number of averages in the CPMG sequence, or further optimize the gradients efficiency based on existing methods [66–68]. A potentially significant eddy current problem is expected to be of minor importance for the non-metallic resonant structure of this work.

Other limiting factors for pulsed mode of operation may be sample heating at high repetition rate and/or decrease of echo amplitude due to diffusion under large gradients. Our initial estimate for these effects is that both of them are not significant. The sample heating is relatively small due to the efficient E/H separation in the ferroelectric-based resonator, and due to the low pulse power required for such resonators (having high C_p [69]). With respect to diffusion, in contrast to NMR, diffusion in the time scale of pulsed ESR does not result in noticeable echo decay, at least for the gradient values considered for 10 μm resolution. However, some echo decay (up to 50%) may occur for the gradients corresponding to 1 μm resolution. This decay can be used as a tool to assess local diffusion and transport phenomena in the sample, similar to the NMR methods.

To summarize this part, at pulsed X-band, the predicted achievable resolution for 1 mM trityl solution is $\sim 5 \times 5 \times 25\,\mu m$ for 64×64 pixels 2D image in less than 1 h of acquisition. At 35 GHz, under similar conditions, one should expect to obtain image resolution of: $\sim 2 \times 2 \times 10\,\mu m$. Further extrapolation to 60 GHz gives SNR results which are only slightly better than those calculated for the CW case at the same frequency, (the frequency dependence is slightly different between the CW and pulse techniques). This means that by employing a typical 3D imaging sequence ([18], see below), a 64×64 pixel 2D image with z slice selection, having resolution of $1 \times 1 \times 10$ μm could be produced for

U-band in less than 1 h. As stated above, we do not see much point in further extrapolating our estimations to higher frequencies. These estimates can be further improved by employing more asymmetric voxels (such as in optical microscopy, which has resolution of $<1\,\mu m$ in XY plane but focal depth of ~30–$100\,\mu m$ along the Z-axis); and by increasing sample concentration to $\sim2\,mM$. It should be noted that although the SNR at U-band is very similar, in the cases we examined, for pulse and CW, the pulse technique is much more versatile, yields better SNR in situations of shorter T_1, and can potentially provide more parameters of interest (transport constants, homogeneous T_2, contrast of T_1, etc., as routinely performed in NMR). The resolution values presented above are derived based on the SNR predictions. However, we anticipate a major technical challenge in producing the required pulsed gradients, and that may ultimately be the limiting factor for resolution in pulsed acquisition, rather than the SNR.

4. Experimental results

In this section, we present our initial experimental imaging results performed by the CW method. The experiments were performed using an X-band spectrometer (Varian E-12) equipped with the imaging probe shown in Fig. 2. The CW imaging probe (an "open" version of the resonator presented recently [69]) is based on double stacked high permittivity rings/discs machined from $SrTiO_3$ single crystal (Commercial Crystals, Florida, permittivity $\varepsilon_r \sim 300$). This non-metallic miniature ($\sim2\,mm$ in diameter and 0.55 mm in height for each ring) structure was selected due to its small size and its "immunity" to the eddy current problem (for future pulsed experiments). The design for the entire resonator and gradient coils was conducted under the constraint that a large ($20 \times 4 \times 0.5$ mm) flat sample could be inserted into the probe. This constraint resulted in lower SNR compared to the case of a single ring resonator [69,70], but with the clear benefit of the ability to examine the samples in an "optical microscopy" manner. The resonator is characterized by a small "active volume" of $\sim1.9\,mm^3$ and efficient E/H field separation. Gradient coils are located at a distance of ~2.5 mm from the sample, yielding high efficiency of up to 2.5 T/(m*A) at a power consumption of ~8 W. The main brass body is water cooled and the resonator rings are cooled by He gas flow to maintain the resonance frequency within the AFC range during the acquisition time.

A field frequency lock (FFL) system maintains the on-resonance condition, even for narrow ($<0.01\,mT$) lines over long acquisition times. The FFL system uses the longitudinal gradient coils to correct for the field changes, by applying to these coils DC bias superim-
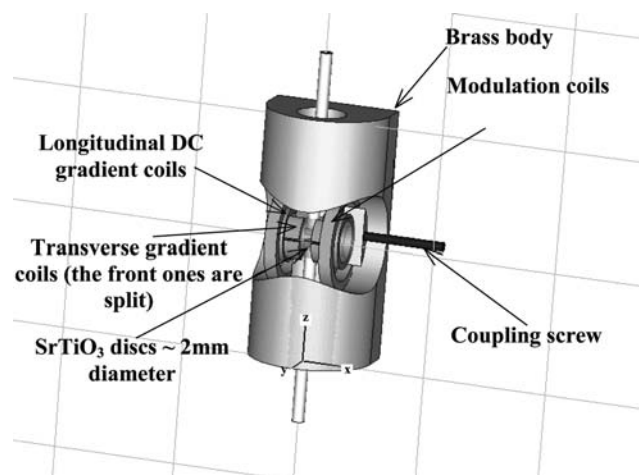

Fig. 2. A drawing of the imaging probe used in this study. The $SrTiO_3$ crystals in the center have dielectric constant of 300 in the microwave region. Consequently, the resonating structure is just 2 mm in diameter at 10 GHz. This greatly improves image resolution and sensitivity. The thin sample is inserted through the slit in the transverse gradient coils to a specified position between the $SrTiO_3$ crystals. The microwaves enter the structure from the rear side. The coupling is adjusted by the capacitive coupling screw in the center of the iris connecting the waveguide to the brass body [69].

posed on the modulated sinusoidal field. The first harmonic of the ESR signal is used as an error signal for the FFL system, while the second harmonic is used as the imaging signal. All of the signal harmonics are available by directly sampling the diode detected signal at a high sampling rate (200 KHz, using National Instruments A/D card 6023E) and analyzing it digitally to obtain the discrete Fourier transform coefficients of the time domain signal [50]. The gradient coils are driven by a sinusoidal current generated digitally in a PC D/A card (model 6711, from National Instruments), with the independent control of current in each of the four coils forming the two gradient coil pairs.

The imaging probe and acquisition algorithms were examined for three typical cases:

(a) *Grid of BDPA radical*. A solid grid of BDPA free radical (α,γ-bisdiphenylene-b-phenylallyl, Aldrich) was prepared by soaking woven Nylon mesh (Goodfellow) with mesh aperture of $50 \times 50\,\mu m$ and wire diameter of $39\,\mu m$ in saturated BDPA solution in toluene and drying out the solvent. The sample was placed between two thin glass cover slides and sealed under nitrogen atmosphere with epoxy glue (Fig. 3, top). The 2D ESR images (Fig. 3, bottom) show sufficient SNR per pixel, but the resolution is limited by the available gradient of ~1–1.5 T/m, which, when combined with the BDPA linewidth of ~0.05–0.1 mT (depending on modulation) results in a resolution of $\sim[50$–$100\,\mu m]^2$ for the second harmonic signal (Eq. (6)). Higher values of gradients could not be reached without losing the AFC lock on the resonator, due to limited heat dissipation of the
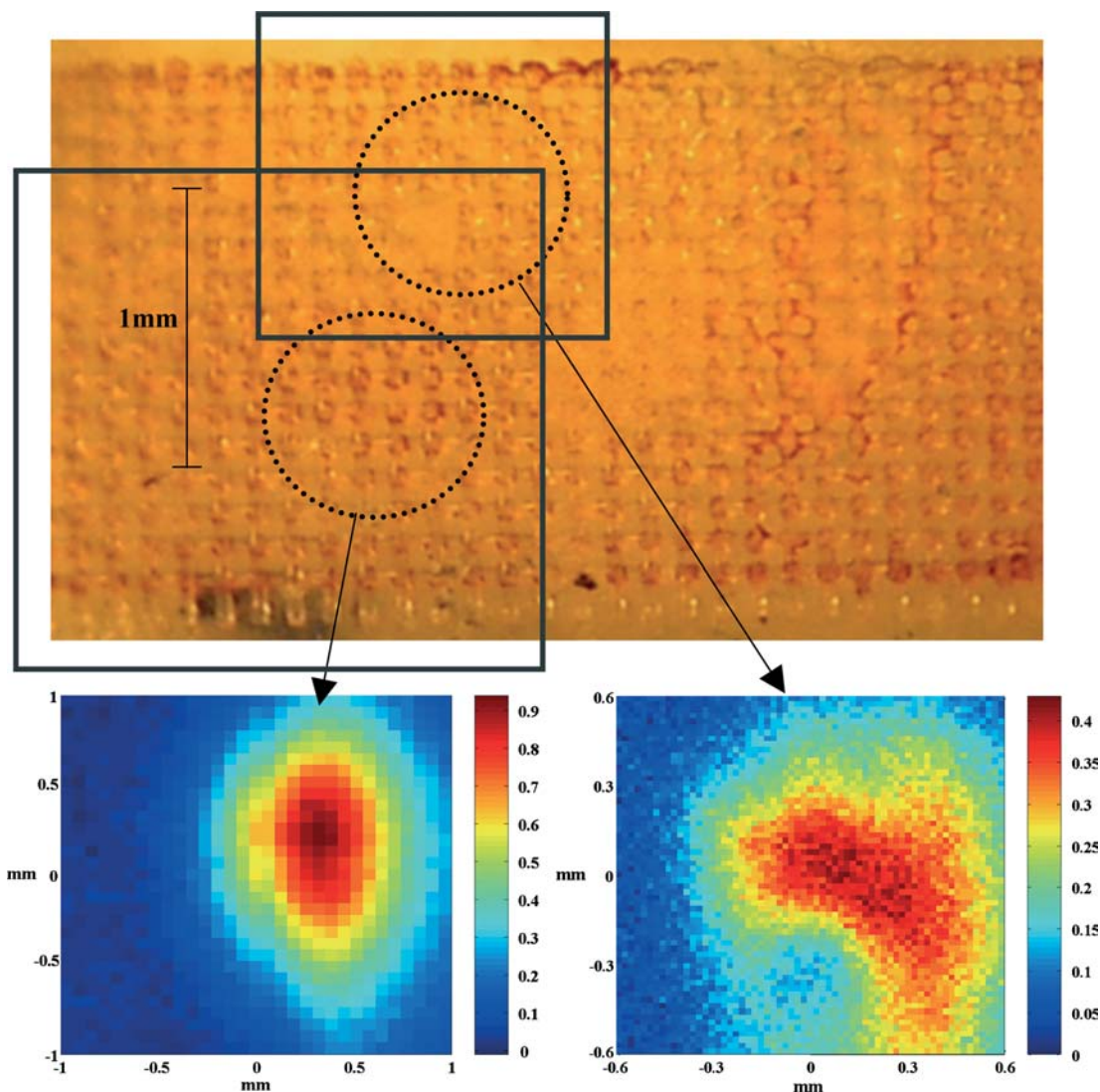
Fig. 3. Images of BDPA grid phantom. Top—the optical image of the phantom with circles marking the active area of the resonator, where signal is depicted by the ESR probe and the squares mark the entire imaged area. Bottom left—a low resolution ESR image of a homogeneous part of the grid, revealing essentially only the sensitive area of the resonator. Bottom right—a higher resolution ($\sim[50{-}100\,\mu m]^2$) ESR image revealing the lack of radicals in part of the grid (due to the effect of cyanoacrylate glue). At this resolution, the Nylon mesh is still not resolved. The vertical color bars represent the relative pixel ESR signal in an arbitrary scale.

modulation coils and the high sensitivity of the ferro-electric resonator frequency to temperature changes [69].

(b) *Trityl solution within the grid.* This liquid sample was prepared by filling the same Nylon mesh mentioned above, with 1 mM protonated trityl (Tris(8-carboxyl-2,2,6,6-tetramethylbenzo-[1,2-*d*;4,5-*d′*]bis[1,3]dithiol-4-yl) tri-sodium salt, courtesy of Prof. Halpern, Chicago Univ.) solution in water (under normal atmosphere). This case relates directly to our calculations of the previous section with respect to SNR and image resolution. In this imaging example (Fig. 4), the narrow linewidth of the trityl radical ($\sim$0.2 G, with modulation) results in a resolution which can be roughly estimated from the image (and corresponds to Eq. (6)) to be $\sim[25\,\mu m]^2$, (see below). The sample thickness is $\sim$100 μm. The image

SNR (pixel signal vs RMS pixel noise) is $\sim$2. These results are consistent with the theoretical predictions (Fig. 1), predicting an SNR of $\sim$12 for a $25 \times 25 \times 100\,\mu m$ voxel (for a resonator with 1.9 mm^3 active volume). The discrepancies that still exist are attributed to the following reasons: (a) the low Q_L of the resonator ($\sim$250 vs. 1000 taken in the calculation, mainly due to the effect of gradient coils and radiation losses); (b) the limitation of the Varian detection system, which prevents working at low power ($\sim$10 μW and less, cf. Fig. 1) due to AFC limitations; (c) the short time constant (32 vs. 100 ms taken in the calculation) used in the data acquisition due to inefficient data handling in the current architecture; (d) the acquisition of the second harmonic signal for the ESR image using the current operation
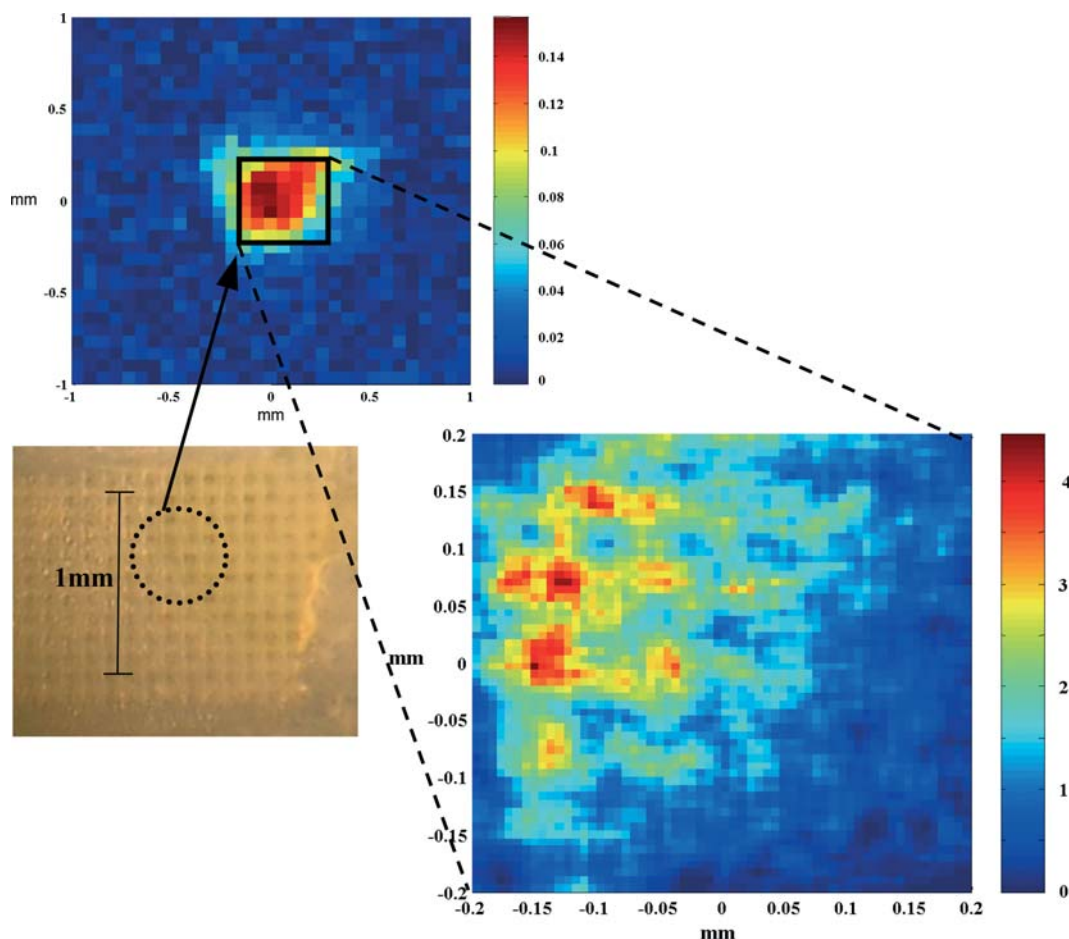
Fig. 4. Images of the Nylon mesh filled with water solution of trityl radical. Upper left—image taken at low resolution, which reveals only the active volume of the resonator, marked with a circle in the optical photo (a double-stacked disc resonator was employed here rather than the double-ring resonator, used in the BDPA case, which caused the active volume to decrease, due to a more confined resonance mode). Lower right—a high resolution image that reveals mainly the trityl within the gaps of the mesh (although water solution exists also above and below the mesh because it is a woven 3D mesh, limiting the contrast of the image). With increased distance from the center of the image, the grid in the ESR image exhibits a slight distortion due to non-planar nodal surface of the modulated gradient fields (this effect can be accounted for and corrected using proper calibration of the gradient fields for a given coil setup). Lower left—optical image of the grid filled with the trityl solution (the sample is almost transparent, but appears here slightly yellow due to the microscope light source). The vertical color bars represent the relative pixel ESR signal in an arbitrary scale.

mode of the FFL system. The second harmonic signal is weaker than the first harmonic (for which the calculations were made) [50].

(c) *LiPc phantom*. A small phantom of LiPc (lithium phthalocyanine radical) crystal was used to examine the resolution limits of the current system, since it has high spin concentration in each voxel (resulting in high SNR) and narrow linewidth, <0.01 mT (under nitrogen atmosphere). Fig. 5 shows a typical imaging result for this sample, when employing gradients of ~ 1.2 T/m. The net image acquisition time (for 64×64 pixels) is 2 min. However, due to limitations of the data acquisition equipment, the experiment takes ~ 15 min. With respect to the image resolution, a reasonable definition for resolution would be: "the smallest distance between two point samples, which still enables them to be resolved separately." However, it is difficult to produce such

"point" samples of spins accurately in the micron scale. Nevertheless, the resolution of the image can be estimated from a 1D cut through the object, similar to what was done in NMR microscopy [2]. Using this method, the resolution of this image is determined to be $\sim [10\,\mu m]^2$–$[15\,\mu m]^2$. These results of resolution and acquisition time are, to our knowledge, the best achieved to-date in 2D ESR imaging.

5. Conclusions

Micron resolution is highly desirable in many important magnetic resonance microscopy applications. Conventional NMR imaging technology is mature but has proven to be limited in the micron scale and probably could not be improved upon easily. ESR imaging
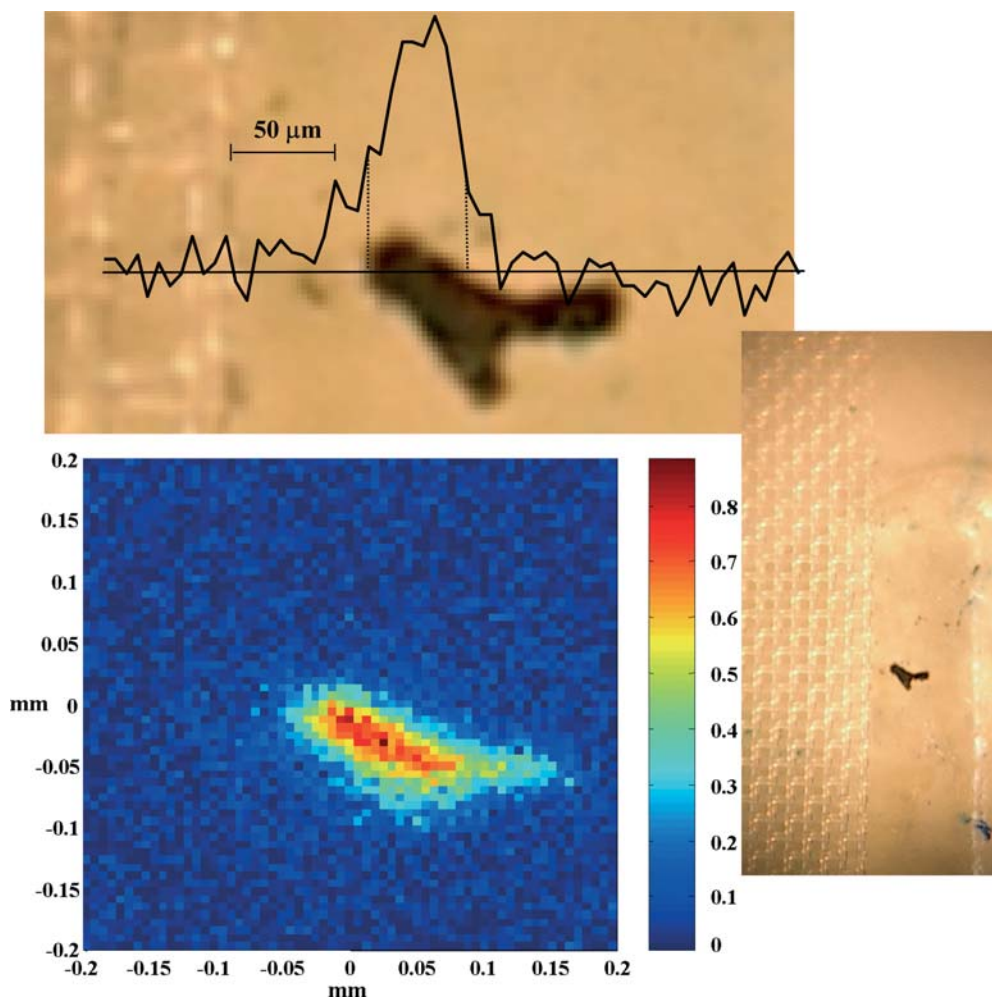
Fig. 5. Image of LiPc phantom. Upper left—high magnification optical image of the phantom, with the appropriate scaling. Right—optical image of the phantom at low magnification, with the Nylon mesh serving as a scale. Lower left—the ESR image. A 1D cut through the ESR image (upper left) is super-imposed on the optical image for clarity. This 1D data were used to evaluate the resolution of the ESR image (cf. text). Notice that the ESR image does not correspond exactly to the optical image. This may be caused by an inhomogeneous distribution of radicals within the phantom (probably due to the effect of the glue which destroyed some of the radicals in the lower part of the phantom). The vertical color bars represent the relative pixel ESR signal in an arbitrary scale.

may provide a solution for the problem of (sub)micron resolution in magnetic resonance imaging. However, existing technology needs to be further developed in terms of resonators, gradient coils, current drivers, fast signal acquisition/processing, and radicals. Backed by our theoretical estimates, we have begun the journey towards the goal of micron resolution. The initial CW ESR 2D image resolution achieved thus far is in line with the theoretical predictions. Current experimental limitations could be overcome in future work, after some necessary improvements. These improvements include: better resonators and gradient coils, efficient heat removal, moving to higher working frequency, and the use of advanced pulsed techniques coupled with efficient signal acquisition systems. All these improvements, that are actively being pursued, should ultimately help to achieve these objectives.

References

[1] P. Callaghan, Principles of Nuclear Magnetic Resonance Microscopy, Oxford University Press, Oxford, 1991.

[2] L. Ciobanu, D.A. Seeber, C.H. Pennington, 3D MR microscopy with resolution 3.7 μm by 3.3 μm by 3.3 μm, J. Magn. Reson. 158 (2002) 178–182.

[3] D.E. Demco, B. Blumich, Solid-state NMR imaging methods. Part I: strong field gradients, Concepts Magn. Reson. 12 (2000) 188–206.

[4] R.E. Botto, G.D. Cody, S.L. Dieckman, D.C. French, N. Gopalsami, P. Rizo, Three-dimensional magnetic resonance microscopy of materials, Solid State Nucl. Magn. Reson. 6 (1996) 389–402.

[5] N. Ishida, M. Koizumi, H. Kano, The NMR microscope: a unique and promising tool for plant science, Ann. Bot. 86 (2000) 259–278.

[6] G.A. Johnson, H. Benveniste, R.D. Black, L.W. Hedlund, R.R. Maronpot, B.R. Smith, Histology by magnetic-resonance microscopy, Magn. Reson. Quart. 9 (1993) 1–30.

[7] G.R. Eaton, S.S. Eaton, Introduction to EPR imaging using magnetic field gradients, Concepts Magn. Reson. 7 (1995) 49–67.

[8] G.L. He, A. Samouilov, P. Kuppusamy, J.L. Zweier, In vivo imaging of free radicals: applications from mouse to man, Mol. Cell. Biochem. 234 (2002) 359–367.

[9] H.M. Swartz, R.B. Clarkson, The measurement of oxygen in vivo using EPR techniques, Phys. Med. Biol. 43 (1998) 1957–1975.

[10] K.I. Yamada, R. Murugesan, N. Devasahayam, J.A. Cook, J.B. Mitchell, S. Subramanian, M.C. Krishna, Evaluation and comparison of pulsed and continuous wave radiofrequency electron paramagnetic resonance techniques for in vivo detection and imaging of free radicals, J. Magn. Reson. 154 (2002) 287–297.

[11] T. Herrling, N. Klimes, W. Karthe, U. Ewert, B. Ebert, Electron-paramagnetic-resonance zeugmatography with modulated magnetic-field gradient, J. Magn. Reson. 49 (1982) 203–211.

[12] T. Herrling, J. Fuchs, N. Groth, Kinetic measurements using EPR imaging with a modulated field gradient, J. Magn. Reson. 154 (2002) 6–14.

[13] Akademie Der Wissenschaften Der DDR, ZZG1 User Manual, DDR, 1987.

[14] W. Karthe, E. Wehrsdorfer, Measurement of inhomogeneous distributions of paramagnetic centers by means of EPR, J. Magn. Reson. 33 (1979) 107–111.

[15] G.R. Eaton, S.S. Eaton, K. Ohno (Eds.), EPR Imaging and Vivo EPR, CRC Press, Boca Raton, 1991.

[16] G.G. Maresch, M. Mehring, S. Emid, High-resolution electron-spin-resonance imaging, Phys. B & C. 138 (1986) 261–263.

[17] A. Coy, N. Kaplan, P.T. Callaghan, Three-dimensional pulsed ESR imaging, J. Magn. Reson. A. 121 (1996) 201–205.

[18] A. Feintuch, G. Alexandrowicz, T. Tashma, Y. Boasson, A. Grayevsky, N. Kaplan, Three-dimensional pulsed ESR Fourier imaging, J. Magn. Reson. 142 (2000) 382–385.

[19] A.I. Smirnov, O.G. Poluectov, Y.S. Lebedev, High-field EPR imaging, J. Magn. Reson. 97 (1992) 1–12.

[20] A.D. Milov, A.Y. Pusep, S.A. Dzuba, Y.D. Tsvetkov, Electron-spin echo as a method of electron-spin-resonance tomography, Chem. Phys. Lett. 119 (1985) 421–425.

[21] G. Boero, P.A. Besse, R. Popovic, Hall detection of magnetic resonance, Appl. Phys. Lett. 79 (2001) 1498–1500.

[22] F. Sakran, A. Copty, M. Golosovsky, N. Bontemps, D. Davidov, A. Frenkel, Electron spin resonance microscopic surface imaging using a microwave scanning probe, Appl. Phys. Lett. 82 (2003) 1479–1481.

[23] D. Rugar, C.S. Yannoni, J.A. Sidles, Mechanical detection of magnetic-resonance, Nature 360 (1992) 563–566.

[24] C. Durkan, M.E. Welland, Electronic spin detection in molecules using scanning-tunneling-microscopy-assisted electron-spin resonance, Appl. Phys. Lett. 80 (2002) 458–460.

[25] D. Hogemann, J.P. Basilion, "Seeing inside the body": MR imaging of gene expression, Eur. J. Nucl. Med. Mol. Imaging 29 (2002) 400–408.

[26] G. Fleige, B. Hamm, C. Zimmer, Molecular MR imaging, Rofo-Fortschritte Auf Dem Gebiet Der Rontgenstrahlen Und Der Bildgebenden Verfahren 172 (2000) 865–871.

[27] P. Wunderbaldinger, A. Bogdanov, R. Weissleder, New approaches for imaging in gene therapy, Eur. J. Radiol. 34 (2000) 156–165.

[28] W. Kockenberger, Functional imaging of plants by magnetic resonance experiments, Trends Plant Sci. 6 (2001) 286–292.

[29] A.I. Smirnov, O.E. Yakimchenko, H.A. Golovina, S.K. Bekova, Y.S. Lebedev, EPR imaging with natural spin probes, J. Magn. Reson. 91 (1991) 386–391.

[30] M. Schara, J. Svetek, M. Nemec, Membrane studies in situ in plant-tissues, Acta Pharmacol. 42 (1992) 273–279.

[31] D.A. Schauer, M.F. Desrosiers, P. Kuppusamy, J.L. Zweier, Radiation dosimetry of an accidental overexposure using EPR spectrometry and imaging of human bone, Appl. Radiat. Isot. 47 (1996) 1345–1350.

[32] S.S. Ishchenko, S.M. Okulov, I.P. Vorona, Spatial distribution of radiation defects in tooth enamel, Phys. Solid State 41 (1999) 1100–1101.

[33] A.A. Romanyukha, M.G. Mitch, Z.C. Lin, V. Nagy, B.M. Coursey, Mapping the distribution of Sr-90 in teeth with a photostimulable phosphor imaging detector, Radiat. Res. 157 (2002) 341–349.

[34] G.A. Watt, M.E. Newton, J.M. Baker, EPR and optical imaging of the growth-sector dependence of radiation-damage defect production in synthetic diamond, Diamond Relat. Mater. 10 (2001) 1681–1683.

[35] K. Kruczala, M.V. Motyakin, S. Schlick, 1D and 2D electron spin resonance imaging (ESRI) of nitroxide radicals in stabilized poly(acrylonitrile–butadiene–styrene) (ABS): UV vs thermal degradation, J. Phys. Chem. B 104 (2000) 3387–3392.

[36] M. Lucarini, G.F. Pedulli, M.V. Motyakin, S. Schlick, Electron spin resonance imaging of polymer degradation and stabilization, Prog. Polym. Sci. 28 (2003) 331–340.

[37] Z. Xiang, Y. Xu, The status quo and prospect of ESR imaging applications to study on catalysts, Appl. Magn. Reson. 12 (1997) 69–79.

[38] M. Ikeya, M. Yamamoto, Electron-spin-resonance image of annealing under thermal-gradient— chemical-vapor-deposition polysilicon film, Jpn. J. Appl. Phys. Part 2 33 (1994) L1087–L1089.

[39] H.J. Halpern, G.V.R. Chandramouli, E.D. Barth, C. Yu, M. Peric, D.J. Grdina, B.A. Teicher, Diminished aqueous microviscosity of tumors in murine models measured with in vivo radiofrequency electron paramagnetic resonance, Cancer Res. 59 (1999) 5836–5841.

[40] M. Petelin, U. Skaleric, P. Cevc, M. Schara, The permeability of human cementum in vitro measured by electron paramagnetic resonance, Arch. Oral Biol. 44 (1999) 259–267.

[41] C.S. Sunandana, Techniques and applications of electron spin resonance, Bull. Mater. Sci. 21 (1998) 1–70.

[42] L.K. Aminov, M.P. Tseitlin, K.M. Salikhov, 1-D EPR imaging of conducting and lossy-dielectric samples, Appl. Magn. Reson. 16 (1999) 341–362.

[43] E.S. Nefedov, K.M. Musin, T.Y. Mirakova, M.K. Kadirov, K.L. Aminov, K.M. Salikhov, V.A. Silaev, EPR imaging study of paramagnetic centre distribution in thiokol-epoxy hermetics, Appl. Magn. Reson. 11 (1996) 115–123.

[44] G. Kordas, Y.H. Kang, 3-Dimensional electron-paramagnetic-resonance imaging technique for mapping porosity in ceramics, J. Am. Ceram. Soc. 74 (1991) 709–713.

[45] M. Ikeya, Electron-spin-resonance (ESR) microscopy in materials science, Annu. Rev. Mater. Sci. 21 (1991) 45–63.

[46] L.J. Berliner, H. Fujii, ESR imaging of polymers and solid materials, Makromol. Chem. Macromol. Symp. 34 (1990) 263–276.

[47] C. Heine, K. Kupferschlager, S. Stapf, B. Blumich, NMR velocimetry of falling liquid films, J. Magn. Reson. 154 (2002) 311–316.

[48] M. Cova, R. Toffanin, MR microscopy of hyaline cartilage: current status, Eur. Radiol. 12 (2002) 814–823.

[49] P.D. Majors, K.R. Minard, E.J. Ackerman, G.R. Holtom, D.F. Hopkins, C.I. Parkinson, T.J. Weber, R.A. Wind, A combined confocal and magnetic resonance microscope for biological studies, Rev. Sci. Instrum. 73 (2002) 4329–4338.

[50] C.P. Poole, Electron Spin Resonance: A Comprehensive Treatise on Experimental Techniques, Wiley, New York, 1982.

[51] The resonator effective volume is defined here by the volume of a single voxel sample in the center of the resonator, divided by the filling factor of this sample.

[52] G.V.R. Wilson, Modulation boadening of NMR and ESR line shapes, J. Appl. Phys. 34 (1963) 3276–3285.

[53] L. Yong, J. Harbridge, R.W. Quine, G.A. Rinard, S.S. Eaton, G.R. Eaton, C. Mailer, E. Barth, H.J. Halpern, Electron spin relaxation of triarylmethyl radicals in fluid solution, J. Magn. Reson. 152 (2001) 156–161.

[54] J.H. Ardenkjaer-Larsen, I. Laursen, I. Leunbach, G. Ehnholm, L.G. Wistrand, J.S. Petersson, K. Golman, EPR and DNP properties of certain novel single electron contrast agents intended for oximetric imaging, J. Magn. Reson. 133 (1998) 1–12.

[55] D.I. Hoult, R.E. Richards, Signal-to-noise ratio of nuclear magnetic-resonance experiment, J. Magn. Reson. 24 (1976) 71–85.

[56] D.I. Hoult, N.S. Ginsberg, The quantum origins of the free induction decay signal and spin noise, J. Magn. Reson. 148 (2001) 182–199.

[57] J. Jeener, F. Henin, A presentation of pulsed nuclear magnetic resonance with full quantization of the radio frequency magnetic field, J. Chem. Phys. 116 (2002) 8036–8047.

[58] G.A. Rinard, R.W. Quine, R.T. Song, G.R. Eaton, S.S. Eaton, Absolute EPR spin echo and noise intensities, J. Magn. Reson. 140 (1999) 69–83.

[59] G.A. Rinard, R.W. Quine, S.S. Eaton, G.R. Eaton, W. Froncisz, Relative benefits of overcoupled resonators vs inherently low-Q resonators for pulsed magnetic-resonance, J. Magn. Reson. A 108 (1994) 71–81.

[60] D.I. Hoult, B. Bhakar, NMR signal reception: virtual photons and coherent spontaneous emission, Concepts Magn. Reson. 9 (1997) 277–297.

[61] A. Blank, H. Levanon, Filling factor in a pulsed electron paramagnetic resonance experiment, Spectrochim. Acta A 58 (2002) 1329–1335.

[62] S. Meiboom, D. Gill, Modified spin-echo method for measuring nuclear relaxation times, Rev. Sci. Instrum. 29 (1958) 688–691.

[63] L.P. Panych, R.V. Mulkern, P. Saiviroonporn, G.P. Zientara, F.A. Jolesz, Non-Fourier encoding with multiple spin echoes, Magn. Reson. Med. 38 (1997) 964–973.

[64] U. Ewert, R.H. Crepeau, C.R. Dunnam, D.J. Xu, S.Y. Lee, J.H. Freed, Fourier-transform electron-spin-resonance imaging, Chem. Phys. Lett. 184 (1991) 25–33.

[65] U. Ewert, R.H. Crepeau, S.Y. Lee, C.R. Dunnam, D.J. Xu, J.H. Freed, Spatially resolved 2-dimensional Fourier-transform electron-spin-resonance, Chem. Phys. Lett. 184 (1991) 34–40.

[66] B.A. Chronik, B.K. Rutt, Constrained length minimum inductance gradient coil design, Magn. Reson. Med. 39 (1998) 270–278.

[67] R. Bowtell, P. Robyr, Multilayer gradient coil design, J. Magn. Reson. 131 (1998) 286–294.

[68] R. Bowtell, A. Peters, Analytic approach to the design of transverse gradient coils with co-axial return paths, Magn. Reson. Med. 41 (1999) 600–608.

[69] A. Blank, E. Stavitski, H. Levanon, F. Gubaydullin, Transparent miniature dielectric resonator for electron paramagnetic resonance experiments, Rev. Sci. Instrum. 74 (2003) 2853–2859.

[70] M. Jaworski, A. Sienkiewicz, C.P. Scholes, Double-stacked dielectric resonator for sensitive EPR measurements, J. Magn. Reson. 124 (1997) 87–96.

[71] P.P. Borbat, R.H. Crepeau, J.H. Freed, Multifrequency two-dimensional Fourier transform ESR: an X/Ku-band spectrometer, J. Magn. Reson. 127 (1997) 155–167.